OPTICA

Picosecond-resolution single-photon time lens for temporal mode quantum processing

Chaitali Joshi,[1,2] Ben M. Sparkes,[3] Alessandro Farsi,[1] Thomas Gerrits,[4] Varun Verma,[5] Sven Ramelow,[6] Sae Woo Nam,[5] and Alexander L. Gaeta[1,*]

[1]Applied Physics and Applied Mathematics, Columbia University, New York, New York 10027, USA
[2]Applied and Engineering Physics, Cornell University, Ithaca, New York 14850, USA
[3]Institute for Photonics and Advanced Sensing (IPAS) and School of Physical Sciences, University of Adelaide, Adelaide, SA, Australia
[4]National Institute of Standards and Technology, Gaithersburg, Maryland 20899, USA
[5]National Institute of Standards and Technology, Boulder, Colorado 80305, USA
[6]Institut für Physik, Humboldt-Universität zu Berlin, Berlin, Germany
*Corresponding author: a.gaeta@columbia.edu

Received 5 August 2021; revised 17 January 2022; accepted 14 February 2022; published 28 March 2022

Techniques to control the spectro-temporal properties of quantum states of light at ultrafast time scales are crucial for numerous applications in quantum information science. In this work, we report an all-optical time lens for quantum signals based on Bragg-scattering four-wave mixing with picosecond resolution. Our system achieves a temporal magnification factor of 158 with single-photon level inputs, which is sufficient to overcome the intrinsic timing jitter of superconducting nanowire single-photon detectors. We demonstrate discrimination of two terahertz-bandwidth, single-photon-level pulses with 2.1 ps resolution (electronic jitter corrected resolution of 1.25 ps). We draw on elegant tools from Fourier optics to further show that the time-lens framework can be extended to perform complex unitary spectro-temporal transformations by imparting optimized temporal and spectral phase profiles to the input waveforms. Using numerical optimization techniques, we show that a four-stage transformation can realize an efficient temporal mode sorter that demultiplexes 10 Hermite–Gaussian (HG) modes. Our time-lens-based framework represents a new toolkit for arbitrary spectro-temporal processing of single photons, with applications in temporal mode quantum processing, high-dimensional quantum key distribution, temporal mode matching for quantum networks, and quantum-enhanced sensing with time-frequency entangled states.

https://doi.org/10.1364/OPTICA.439827

1. INTRODUCTION

Photonic quantum information processing (QIP) using temporal modes of light requires coherent manipulation and detection of picosecond and sub-picosecond scale temporal waveforms at the single-photon level. Such coherent reshaping of the spectro-temporal properties of quantum optical waveforms is also necessary for several applications such as efficient storage and retrieval of single-photon wave packets from matter-based quantum memories and photonic cavities [1–5], temporal mode matching for quantum networks [6–8], controlling time-frequency entanglement at ultrafast time scales [9,10], and the generation of high-bandwidth squeezed light [11–13]. Single-photon pulses in well-defined temporal modes are ideal for applications that require active synchronization in the time domain such as quantum key distribution and distributed computing [14]. Moreover, high-dimensional qudits encoded in time, frequency, and time-frequency domains greatly improve the information carrying capacity and noise resilience of quantum communication channels as compared to binary encoding [15,16]. By combining techniques such as pulse shaping with parametric nonlinear processes such as three- and four-wave mixing (FWM), a complete set of operations has been proposed including generation, coherent operations, and tomography of orthogonal temporal modes of quantum light [17–24]. In addition, techniques such as ultrafast gating have been used to directly characterize time-energy entangled photons [9,25]. However, far more complex and generalized unitary transformations are necessary to fully harness the potential of temporal modes of light for quantum applications.

Here, we demonstrate an alternative route for processing picosecond-scale single-photon waveforms using a time lens. Drawing on space-time duality [Fig. 1(a)], temporal imaging systems ("time lens") have been used for the generation and direct characterization of complex, ultrafast classical pulses with bandwidths >1 THz [26–30]. Time-lens-based systems have also been used for manipulating the bandwidth and spectral correlations of single photons using electro-optic modulators (EOMs) and three-wave mixing, respectively [31–33]. In this work, we realize a time-lens system based on coherent, noise-free manipulation of single-photon level pulses via Bragg-scattering four-wave mixing

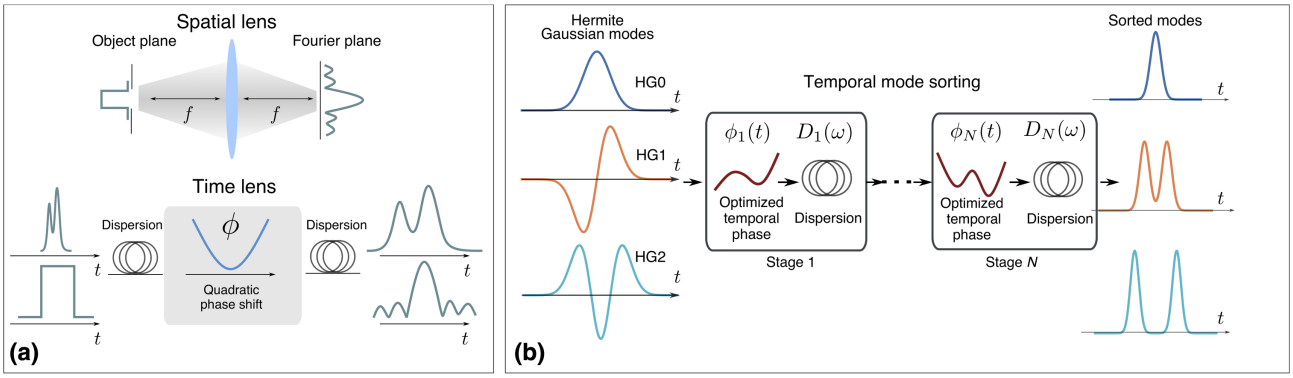

Fig. 1. Temporal mode processing with time-lens systems. (a) Analogous to a spatial lens, a time lens imparts a quadratic temporal phase to the input signal. By using suitable dispersion before and after the time lens, a complete imaging system capable of performing magnification, compression, or Fourier transforms in the time domain is possible. (b) Schematic for temporal mode sorting. By imparting optimized temporal and spectral phase profiles, complex, generalized unitary transformations in the time-frequency domain can be realized. The cascaded operations form a multimode linear interferometer that performs a basis transformation in the time domain and simultaneously demultiplexes intensity overlapping, field-orthogonal Hermite–Gaussian (HG) modes.

(BS-FWM). Using a combination of pulsed and continuous wave (cw) pumps in the nonlinear interaction, we engineer BS-FWM to achieve broadband phase matching with an acceptance bandwidth of more than 1 THz. Our system achieves a temporal magnification factor of 158, and we demonstrate discrimination of two single-photon level pulses with a resolution of 2.1 ps (electronic jitter corrected resolution of 1.25 ps). Further, drawing on elegant tools from Fourier optics [34–36], we propose extending the applications of time-lens-based systems to perform complex unitary transformations on temporal modes. In the spatial domain, tools from Fourier optics, such as coordinate transformations, have been used for the generation and efficient detection of orbital angular momentum (OAM) eigenstates of light [35,37,38]. We show that these techniques can be generalized to the time domain by imparting optimized temporal and spectral phase profiles on the pulsed pump involved in the nonlinear process. In particular, we numerically demonstrate a four-stage temporal mode sorter that efficiently demultiplexes 10 Hermite–Gaussian (HG) modes [Fig. 1(b)]. These cascaded temporal and spectral phases realize a linear, multimode interferometer that performs a basis transformation in the time domain [39]. This interpretation is powerful and provides a new toolkit for arbitrary processing of temporal modes of quantum light.

All-optical processing of quantum light using the time-lens paradigm has several advantages. By directly harnessing nonlinear optical processes, time-lens systems based on wave mixing can support large bandwidths up to a few THz. EOMs typically have a limited bandwidth of a few 10s of GHz and an insertion loss of a few dB. Using a dispersion-shifted fiber as the nonlinear medium, our implementation of BS-FWM achieves flexible phase matching with an acceptance bandwidth of more than 1 THz and an insertion loss of just 1.3 dB [40–43]. The quadratic temporal phase is imparted to the photons via the chirped BS-FWM pump, reducing the total loss in the path of the photons due to dispersive elements and 4 f-waveshapers. Moreover, the $\chi^{(3)}$ nonlinearity allows for an all-fiber implementation, and the use of two pumps makes it possible to achieve frequency translation between closely spaced frequency modes [44,45]. This can prove advantageous in terms of experimental complexity, as $\chi^{(2)}$ processes typically impart large frequency shifts with the input and target modes placed in different optical bands.

2. SINGLE-PHOTON TIME LENS USING BRAGG-SCATTERING FOUR-WAVE MIXING

Our scheme for implementing a temporal imaging system using BS-FWM is shown in Fig. 2. BS-FWM is a third-order nonlinear process where two undepleted pumps mediate the interaction between two single-photon level fields [44,46–48]. Using a commercially available dispersion-shifted fiber as the nonlinear medium, we have previously demonstrated that BS-FWM can be used to achieve quantum frequency conversion of quasi-cw inputs with near-unity efficiency and low added noise [41–43]. The frequency separation between the pump fields can be tuned to more than 1.7 THz to achieve frequency conversion over large bandwidths [42]. These flexible phase-matching conditions can be exploited to use BS-FWM with pulsed, single-photon level inputs.

We use a configuration where one of the pumps, centered at ω_{P1}^0, is pulsed, and the other pump (ω_{P2}^0) is cw. A quadratic temporal phase (linear frequency chirp) is imparted on the pulsed pump. The pumps and single-photon fields are placed symmetrically about the zero group-velocity dispersion (GVD) wavelength of the nonlinear medium. Below, we derive conditions under which the broadband input centered at ω_R^0 is converted to a narrow field centered at ω_B, which corresponds to spectral compression (temporal magnification) of the input pulse. We assume group-delay dispersions (GDDs, $\beta^{(2)}L$) of Φ_{P1}, Φ_R are imparted on the pulsed fields centered at ω_{P1}^0, ω_R^0, respectively. The GDD introduces a phase $\exp(\frac{i\tau^2}{2\Phi})$ [26]. For a Gaussian pulse, the chirp induced by this dispersion is linear, and in the limit of large chirp on the two pulsed fields ($\Phi\delta\omega^2 \gg 1$, $\delta\omega$, pulse bandwidth), we can express the instantaneous frequency of the pulsed fields as $\omega_{P1}(\tau) = \omega_{P1}^0 + \tau/\Phi_{P1}$ and $\omega_R(\tau) = \omega_R^0 + \tau/\Phi_R$ [49]. For convenience, we introduce variables for the frequency separation of the two pumps $\Omega = \omega_{P1}^0 - \omega_{P2}^0$, and $\tilde{\omega}$ for the frequency separation of the pumps from the zero-GVD point ω_{ZGVD} [Fig. 2(a)]. Using energy conservation, the frequencies of the interacting fields can be written as

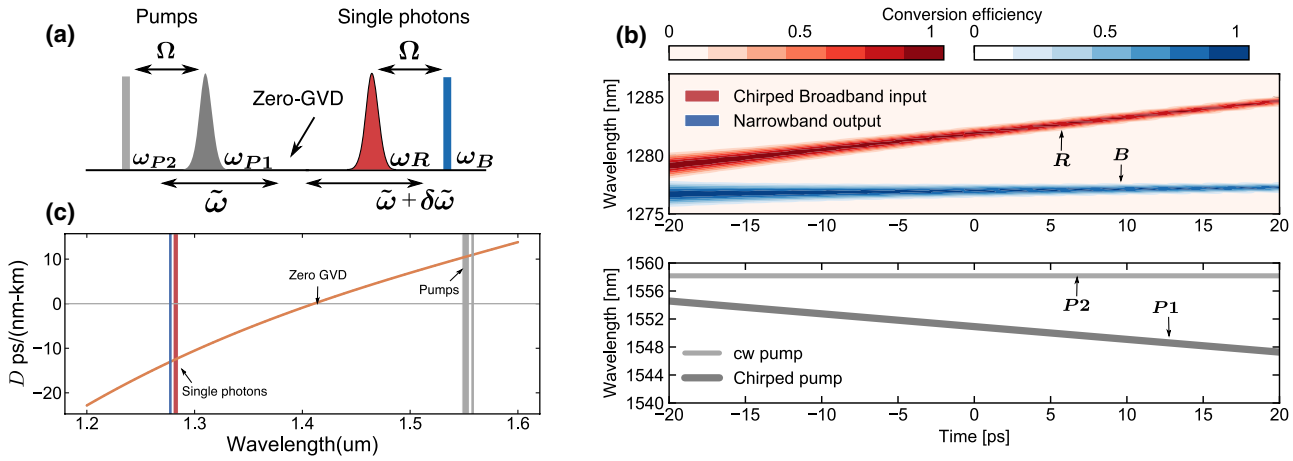

Fig. 2. Time lens via Bragg-scattering four-wave mixing (BS-FWM). (a) One of the BS-FWM pumps (ω_{P1}) is pulsed with a quadratic temporal phase (linear frequency chirp, Φ_{P1}), and the other pump field (ω_{P2}) is cw. A broadband, single-photon level input (ω_R) with chirp Φ_R is converted to a narrow output field centered at ω_B when the phase-matching condition is satisfied. The pump and single-photon fields are placed symmetrically about the zero group-velocity dispersion (GVD) point of the fiber. (b) Broadband phase matching is achieved when the chirp applied to the two pulsed fields are equal in magnitude and opposite in sign ($\Phi_{P1} = -\Phi_R$). The broadband input (red) is converted to the narrow, unchirped output shown in blue. For measured dispersion parameters of the nonlinear medium, the acceptance bandwidth of this process exceeds 1 THz (5.5 nm), corresponding to picosecond-scale temporal resolution. (c) Measured dispersion profile of the BS-FWM fiber.

$$\omega_{P1}(\tau) = \omega_{\mathrm{ZGVD}} - \tilde{\omega} + \frac{\Omega}{2} + \frac{\tau}{\Phi_{P1}},$$

$$\omega_{P2}^{0} = \omega_{\mathrm{ZGVD}} - \tilde{\omega} - \frac{\Omega}{2},$$

$$\omega_R(\tau) = \omega_{\mathrm{ZGVD}} + \tilde{\omega} + \delta\tilde{\omega} - \frac{\Omega}{2} + \frac{\tau}{\Phi_R},$$

$$\omega_B(\tau) = \omega_{\mathrm{ZGVD}} + \tilde{\omega} + \delta\tilde{\omega} + \frac{\Omega}{2} + \frac{\tau}{\Phi_{P1}} + \frac{\tau}{\Phi_R}. \quad (1)$$

Here, $\delta\tilde{\omega}$ is a small frequency offset necessary to compensate for effects of higher-order dispersion (see Fig. 2 and Supplement 1, Section S1). The instantaneous phase mismatch $\Delta\beta = \beta_{P1} - \beta_{P2} + \beta_R - \beta_B$, ($\beta$, propagation constant) can be Taylor expanded about the zero-GVD point ($\beta^{(2)}(\omega_{\mathrm{ZGVD}}) = 0$). In the limit $\delta\tilde{\omega} \ll \tilde{\omega}$, the phase mismatch is given by

$$\Delta\beta(\tau) = -\frac{\beta^{(3)}}{2\Phi_R^2\Phi_{P1}^2}\tau(\tau + \Omega\Phi_{P1}) \times (\Phi_{P1} + \Phi_R)(\tau + 2\tilde{\omega}\Phi_R) + \mathcal{O}(\beta^{(4)}). \quad (2)$$

Here, $\beta^{(3)}$ and $\beta^{(4)}$ are third- and fourth-order dispersion coefficients, respectively, evaluated at the zero-GVD point ω_{ZGVD}. From Eq. (2), it is seen that broadband phase matching is possible when the two pulsed fields have equal and opposite chirps ($\Phi_R = -\Phi_{P1}$). Under these conditions, the broadband chirped input ω_R is converted to an unchirped, narrowband output ω_B [Eq. (1)]. Figure 2 shows the calculated conversion efficiency using the measured dispersion parameters for our fiber, including effects of higher-order terms. Efficient conversion can be achieved over a bandwidth exceeding 1 THz (5.5 nm at 1280 nm). Due to $\beta^{(4)}$, the output ω_B acquires a small linear chirp (see Supplement 1, Section S1). The acceptance bandwidth of the time lens is given by $\Delta\omega_{\mathrm{BS}} = -3\Delta\omega_B\beta^{(3)}/\beta^{(4)}\tilde{\omega}$, where $\Delta\omega_B$ is the bandwidth of the output filter (Supplement 1, Section S1). Using the parameters for our experimental system, $\beta^{(3)} = 9.4 \times 10^{-2}$ ps^3/km, $\beta^{(4)} = -2 \times 10^{-4}$ ps^4/km, $\tilde{\omega} = 2\pi \times 19$ THz, and $\Delta\omega_B = 2\pi \times 100$ GHz, we obtain $\Delta\omega_{\mathrm{BS}} = 1.2$ THz. This acceptance bandwidth determines the shortest pulse that can be resolved by our temporal imaging system and corresponds to picosecond temporal resolution.

3. EXPERIMENTAL SETUP

Our experimental setup to implement a time lens based on BS-FWM is shown in Fig. 3. In order to maximize the efficiency of the nonlinear process, we generate an ultrashort input signal pulse that is temporally synchronized with the BS-FWM pulsed pump, as shown in Fig. 4. We spectrally broaden a seed pulsed laser (center wavelength 1560 nm, 80 fs nominal pulse width, 70 mW average power, 80 MHz repetition rate) in a highly nonlinear fiber (HNLF). The resulting spectrum is shown in Fig. 4. We extract the signal centered at 1285 nm using a monochromator (3 dB bandwidth of 5.5 nm). The input signal pulse is sent through a 4-km-long single-mode fiber (OFS Truewave) to impart a GDD $\Phi_s = 7.6$ ps^2 to the input signal. The remaining power from the pulsed laser is sent to a waveshaper (Finisar) for amplitude and phase filtering. We apply a flat-top amplitude filter centered at 1550 nm with a quadratic phase (GDD $\Phi_P = -7.6$ ps^2) to the pump so that the condition $\Phi_P = -\Phi_s$ is satisfied. The signal is passed through a free-space delay line comprising a 60 cm dovetail rail fitted with a corner cube and an additional precision tunable delay line for fine delay control. The tunable delay line is controlled by a servo motor controller (Thorlabs Kinesis). The signal is attenuated by more than 75 dB to the single-photon level, and then combined with the chirped pump and sent to the BS-FWM fiber. For the pulse discrimination measurement, a 2-m-long polarization-maintaining (PM) fiber is introduced in the path of the signal photons. The strong birefringence of the PM fiber results in the creation of two pulses separated by picosecond-scale delay. To generate a synchronized trigger signal, a small band

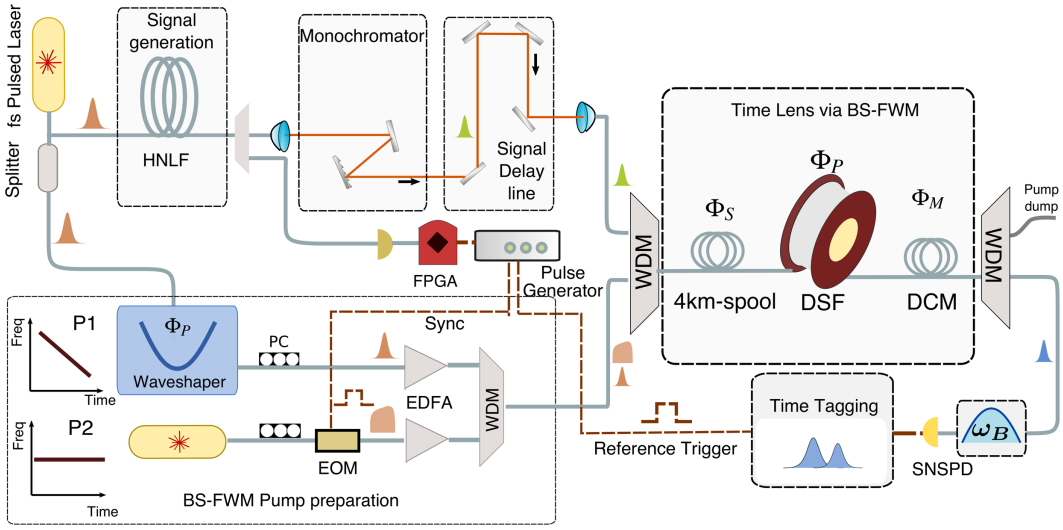

Fig. 3. Experimental setup for temporal magnification using BS-FWM. A fs pulsed laser is spectrally broadened in a highly nonlinear fiber (HNLF) to generate input signal pulses that are temporally synchronized with the pulsed Bragg scattering four-wave mixing BS-FWM pump. The signal pulse centered at 1285 nm (bandwidth 5.5 nm) is extracted using a monochromator, passed through a tunable free-space delay line, attenuated to the single-photon level and sent through 4 km of single-mode fiber, imparting a GDD Φ_s. Two pulses with picosecond-scale delay are generated using a 2 m long polarization-maintaining fiber (not shown). To generate the chirped, broadband pump, about 5% of the power from the fs laser is sent to a waveshaper to impart a controlled GDD and then is amplified with an erbium-doped fiber amplifier (EDFA). A downsampled 10 ns trigger signal synchronized with the pulsed laser is used to modulate the cw pump via an electro-optic modulator (EOM). The pump waves are combined with the chirped input signal using wavelength division multiplexers (WDMs) and sent to the dispersion-shifted fiber (DSF) for BS-FWM. After pump rejection, a dispersion-compensation module (DCM) is used to impart a large GDD (Φ_M) to magnify the output pulses. The magnified pulses are detected using superconducting nanowire detectors (SNSPDs). FPGA, field-programmable gate array.

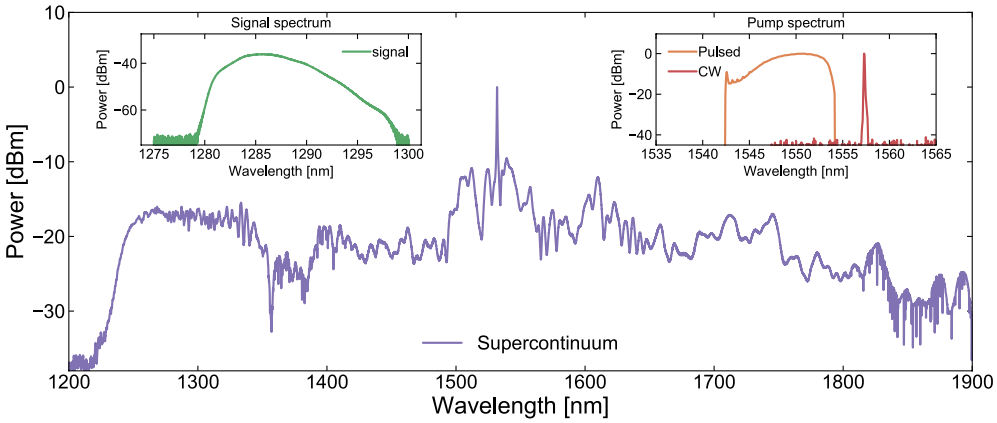

Fig. 4. Generation of temporally synchronized signal pulse. Generated spectrum from spectral broadening of the fs pulsed laser (80 fs nominal pulse width, 1560 nm center wavelength) in a highly nonlinear fiber. Using a monochromator, a portion of this generated supercontinuum with 5.5 nm 3 dB bandwidth is extracted to form the signal (see left inset). The spectrum of the pulsed and cw BS-FWM pumps is shown in the inset on the right.

of the rejected supercontinuum is monitored on a fast photodiode (EOT 3500 F). The photodiode signal is amplified with a high-bandwidth three-stage RF amplifier (Centellax) and then downsampled to 4 MHz using a field-programmable gate array (FPGA). The downsampled signal is used as a trigger to carve out 10 ns pulses from a cw laser at 1558.1 nm using an EOM, which acts as the second pump in the BS-FWM process. For efficient FWM, the pulsed pump and the input signal must be precisely overlapped in time. We observe the delay between the two pulses after the BS-FWM fiber and adjust the signal delay line to achieve a crude overlap of the two pulses. We then scan the tunable delay line to maximize the FWM conversion efficiency. The signal is then passed through a dispersion compensation module (DCM, Corning DCM-80-SMF-C, measured GDD $\Phi_M = 1160\ \text{ps}^2$ at 1280 nm, 8 dB insertion loss). A copy of the downsampled signal is used as a start trigger to the time-tagging module (TTM), and the converted idler pulses are detected using superconducting nanowire single-photon detectors (SNSPDs).

4. EXPERIMENTAL RESULTS

A. Temporal Magnification

In order to measure the magnification factor of our temporal imaging system, we scan the relative delay between the signal and the pulsed BS-FWM pump using the precision tunable delay line and observe the magnified delay with the SNSPDs. This measurement is analogous to moving an object orthogonally to the optical axis of

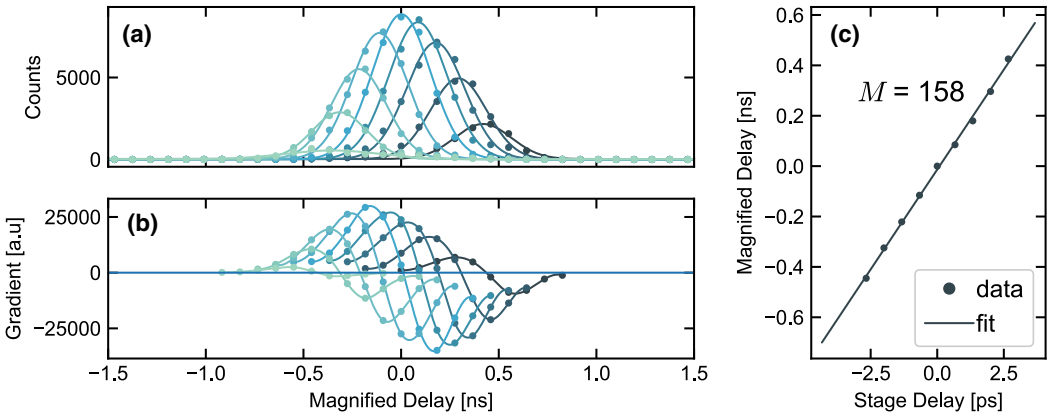

Fig. 5. Magnification of temporal delay. (a) The delay of the input signal is scanned relative to the pulsed BS-FWM pump, and the magnified delay is observed directly on the single-photon detectors. (b) The gradient of the shifted peaks are calculated to accurately calibrate the magnified delay with respect to the actual stage delay. (c) Calibration of the measured magnified delay relative to the actual stage delay results in a measured magnification factor of 158 for our temporal imaging system.

a spatial lens and measuring the corresponding shift in the imaging plane. We record histograms of the arrival time of the photons at the SNSPDs relative to a downsampled electronic trigger signal synchronized with the pulsed laser. Figure 5 shows our results from this measurement. The gradient of the shifted peaks is calculated to accurately calibrate the magnified delay with respect to the actual stage delay. We measure a magnification factor of 158, as shown in Fig. 5. The GDD of the DCM module at 1280 nm is measured separately to be 1160 ps^2 by scanning the frequency of a modulated, attenuated cw laser and measuring the corresponding time delay on the SNSPDs. Our measured magnification factor is in close agreement with the theoretical value $M = |\frac{\Phi_M}{\Phi_s}| = 153$, obtained from the GDD measurements before and after the time lens.

B. Picosecond Pulse Discrimination

We demonstrate pulse discrimination of two single-photon level pulses at the picosecond time scale. For this measurement, we introduce a 2-m-long PM fiber in the path of the single photons. As a result of the birefringence of the PM fiber, two pulses separated with picosecond-scale delay are created. The two pulses are magnified with our time-lens system and observed directly on the SNSPDs, as shown in Fig. 5(a). From the measured magnified pulse width (full width at half-maximum, FWHM = 326 ps) and the calibrated magnification factor ($M = 158$), we infer that the input pulse width is at most 2.1 ps. The two pulses, initially separated by 2.8 ps and unresolvable by direct detection, can now be discriminated with the time lens. For all measurements, we ensure minimal chirp on the generated idler output right after the BS-FWM process by optimizing the GDD imparted to the BS-FWM pump using the waveshaper to precisely match the signal chirp at the input ($\Phi_P = -\Phi_s$).

The measured resolution of our time lens system is primarily limited by the electronic jitter of our measurement system. The most significant contributions are from the synchronized trigger signal used as a reference in our histogram measurements and the intrinsic jitter of the TTM. We characterize the intrinsic jitter of the TTM by measuring the autocorrelation of a fast electronic signal from a delay generator (Stanford Research). The FWHM of the measured autocorrelation signal is $\tau_{\mathrm{ttm,ttm}} = \sqrt{2} J_{\mathrm{ttm}} = 76$ ps [see Fig. 6(b)]. From this value, we extract the single-channel jitter of the TTM to be $J_{\mathrm{ttm}} = 54$ ps. Next, we determine the electronic jitter of the trigger signal by sending the attenuated pulsed laser (80 fs nominal pulse width) to the SNSPDs via a short single-mode fiber to introduce minimal dispersion and measure the cross correlation of the trigger signal with this optical signal using the TTM [see Fig. 6(c)]. The measured FWHM for this cross correlation signal is $\tau_{\mathrm{trig,snspd}} = 260$ ps. Assuming the jitter is modeled by a Gaussian distribution, the combined timing jitter for this measurement can be written as

$$\tau^2_{\mathrm{trig,snspd}} = J^2_{\mathrm{fs-pulse}} + J^2_{\mathrm{snspd}} + J^2_{\mathrm{trig}} + 2J^2_{\mathrm{ttm}}. \tag{3}$$

The timing jitter of the optical pulse, $J_{\mathrm{fs-pulse}}$, is negligible since we are using a fs pulsed laser as the input. The nominal jitter of our SNSPDs is $J_{\mathrm{snspd}} = 70$ ps, and using the measured jitter of the TTM module (54 ps), we determine the jitter of the trigger signal from Eq. (3) to be $J_{\mathrm{trig}} = 238$ ps. This trigger signal jitter is the result of the combined timing jitter of the photodiode, RF amplifier, and FPGA latency.

Having isolated the effects of electronic jitter, we can now determine the resolution of our temporal imaging system. Figure 6 shows a cross correlation between the magnified optical pulse from the time lens detected using the SNSPD and the downsampled trigger signal from the FPGA. The combined jitter for this measurement is

$$\tau^2_{\mathrm{total}} = \tau^2_{\mathrm{mag-pulse}} + J^2_{\mathrm{snspd}} + J^2_{\mathrm{trig}} + 2J^2_{\mathrm{ttm}}, \tag{4}$$

where $\tau_{\mathrm{mag-pulse}}$ is the FWHM of the magnified optical pulses. The FWHM of the measured cross correlation in Fig. 6 is $\tau_{\mathrm{total}} = 326$ ps. From Eqs. (4) and (3), we extract the width of the magnified pulse $\tau_{\mathrm{mag-pulse}}$ to be $\tau_{\mathrm{mag-pulse}} = 198$ ps. From this, we extract the resolution of the lens to be $\tau_{\mathrm{mag-pulse}}/M = 1.25$ ps. This resolution is limited by the width of the input signal pulse, which is determined by the filtering bandwidth and possible additional chirp arising from the setup, non-unitary conversion efficiency due to the temporal shape of the pulsed pump, and residual chirp of the idler due to higher-order dispersion effects (see Fig. 2). The resolution of our current measurement can be significantly improved by using a faster downsampling signal to reduce electronic jitter. Commercial TTMs with an electronic jitter of less

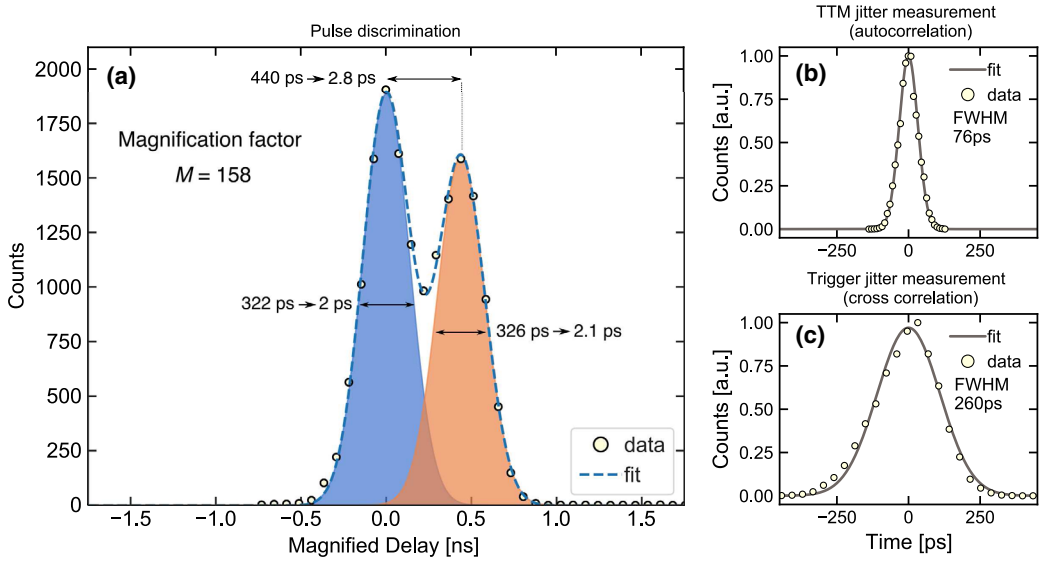

Fig. 6. Pulse discrimination with picosecond resolution. (a) The input signal is sent through a polarization-maintaining fiber to create two pulses with a small relative delay. The two pulses are magnified and directly discriminated on the superconducting nanowire single-photon detectors. Based on the measured magnified pulse width and the calibrated magnification factor of the time lens, the input pulse width is estimated to be at most 2.1 ps. The two pulses, initially separated by 2.8 ps and unresolvable by direct detection, can now be discriminated with the time lens. (b) Measured TTM jitter via autocorrelation using a fast electronic signal. (c) Measured trigger jitter via cross correlation of trigger signal with an ultrashort optical pulse incident on the SNSPDs. These measurements are used to isolate the effects of electronic jitter in our measurement system.

than 5 ps are now widely available. Together with SNSPDs with improved timing resolution [50,51], sub-picosecond resolution can be achieved with our time-lens system.

In order to use our time lens system with single-photon states, it is necessary to minimize system losses and ensure low added noise due to the BS-FWM pumps. We measure a low insertion loss of 1.3 dB for the BS-FWM "time lens" used in our experimental scheme, including the 100 m spool of the BS-FWM fiber (Corning Vistacor), the input WDMs used to combine the signal at 1.28 μm with the pumps at 1.55 μm, and the output WDMs and fiber-based filters for pump rejection (Supplement 1, Section S2 and Fig. S3). All fiber components are spliced to minimize losses. For the temporal magnification setup, the fiber used to impart GDD before the time lens adds 1.4 dB loss (4 km SMF fiber, OFS Truewave, nominal loss 0.35 dB/km) and the DCM (Corning DCM-80) used to impart a large magnification after the time lens adds 8 dB loss (measured). We note that, since the converted idler output is narrowband (0.5 nm bandwidth), this DCM module can be replaced with commercially available chirped fiber Bragg gratings, which can impart a large GDD with significantly reduced loss (see Supplement 1, Section S2).

In order to ensure low added noise due to the BS-FWM pumps, we suppress noise due to spontaneous Raman scattering at the signal wavelength by cooling the fiber in liquid nitrogen (see Supplement 1, Fig. S2a). We measure a signal-to-noise ratio of 43 (16 dB) for the converted narrowband idler mode (Supplement 1, Fig. S2b). This SNR is limited by leakage of the broadband, chirped input signal (Fig. 4, left inset) into the bandwidth (0.5 nm) of the converted narrowband idler mode and can be improved with sharper spectral filtering at the input stage. The measured SNR of the converted output is comparable to that of the input signal (see Supplement 1, Fig. S2c), indicating a large internal conversion efficiency. These measurements suggest that our scheme is suitable for applications with single-photon input states. We note that other parasitic nonlinear processes that can potentially degrade the internal conversion efficiency of BS-FWM are suppressed by the selective phase-matching condition of our scheme [Eq. (2)].

5. TEMPORAL MODE SORTING

Our experimental demonstration shows that BS-FWM can be used as a tool to process single-photon level temporal waveforms on picosecond time scales. The time lens imparts a quadratic phase shift $\phi(t) = \frac{t^2}{2\Phi_p}$ in time on the input temporal waveform, and this operation can be used to perform a Fourier transform just as in the case of a spatial thin lens. A significantly richer set of operations is possible by using complex temporal $\phi(t)$ and spectral $D(\omega)$ phase profiles [36]. High-resolution spatial light modulators (SLMs) can be been used to impart arbitrary transverse phase profiles in the spatial domain. These tools from Fourier optics have proven to be particularly useful for QIP with OAM states of light. Recently, a seven-stage multi-plane light conversion device (MPLC) was used to demonstrate simultaneous sorting of 210 Laguerre–Gaussian (LG) modes [36].

Here, we propose an alternative method for temporal mode sorting and demultiplexing using the time-lens paradigm. HG modes, which form a complete orthogonal basis set, have field-orthogonal but intensity overlapping spectra [10]. This makes it challenging to efficiently sort temporal modes by direct observation of the spectra [17]. Current approaches for temporal mode sorting, such as the quantum pulse gate and temporal mode interferometry, are based on the temporal mode selectivity of quantum frequency conversion [17,19,52]. However, in order to realize an arbitrary N-mode demultiplexer using this scheme, at least N cascaded sorting stages are necessary. Here, we present a numerical simulation of a four-stage mode sorter for $N = 10$ HG input modes. As noted in [39], sorting of orthogonal modes of light can be viewed as a unitary basis transformation that can be performed

with a linear optical network with sufficient degrees of freedom. This framework provides a simplified and significantly more general approach to the challenging problem of mode sorting. Using the time-lens framework, it is possible to realize such a unitary spectro-temporal transformation that simultaneously sorts the input modes, instead of sorting them one by one. Analogous to spatial mode sorting schemes, our approach exploits the inherent structure of the HG basis modes and can reduce the resources required for an experimental realization of the temporal mode sorter with a large number of input modes.

Our scheme is shown in Fig. 7. The input ψ_0^N is the basis set $\mathrm{HG}_0, \mathrm{HG}_1, \mathrm{HG}_2 \ldots \mathrm{HG}_N$ of orthogonal 1D HG modes. The target output is a series of temporally separated Gaussian pulses (see Fig. 8). The "mode sorter" consists of several cascaded stages imparting phase $\phi_i(t)$ and dispersion $D_i(\omega)$ to the input waveforms. We use the loss function,

$$e = 1 - \frac{1}{S}\frac{1}{N}\sum_{i=1}^{S}\sum_{k=1}^{N} |\langle \psi_{i,b}^k | \psi_{i,f}^k \rangle|^2, \tag{5}$$

where (f, b) denote the forward and backward propagated waveforms, respectively, N denotes the number of input HG modes, and S is the total number of optimization stages. The loss function in Eq. (5) captures the waveform mismatch for forward and backward propagation at each stage. We use steepest gradient descent (GD) to calculate the parameters determining $\phi_i(t)$ and $D_i(\omega)$. Another approach to optimization in such problems is the Gerchberg–Saxton phase retrieval algorithm, which strictly enforces wavefront matching at each stage [36]. For single-stage optimization, this algorithm is similar to performing a GD search. For multi-stage optimization, GD guided by the loss function Eq. (5) together with use of regularization terms offers better control over the optimization process and results in faster convergence to a solution. In order to contain the magnitude of the functions ϕ and D and minimize phase-discontinuities during the optimization process, we use regularization terms proportional to the magnitude of the coefficients in ϕ and D. These regularization terms are added to the loss function in Eq. (5). We restrict $D_i(\omega)$ to second-order dispersion for all stages, which is analogous to free-space propagation in the spatial domain. We implement GD using the open source library PyTorch designed for optimizing deep neural networks that allows for fast computation of gradients of the loss function with respect to a large number of optimization parameters. Our optimization converges quickly after about 1000 iterations. The results are shown in Fig. 8. We use four cascaded stages for sorting 10 orthogonal 1D HG modes. The optimized phases determined by GD are shown in Fig. 7. The optimization results in an average overlap of 93% for the forward and backward propagated modes across all stages. The temporally separated Gaussian modes shown in Fig. 8 can be temporally magnified and directly observed using SNSPDs, completing the sorting process. The fast varying temporal phases shown in Fig. 7 can be implemented via cross-phase modulation (XPM) at the pump wavelength [7]. Alternatively, a simplified approach is to use only quadratic temporal ($\phi(t) \propto t^2$) phases for performing Fourier transforms, interleaved between stages of generalized frequency transformations, which can be easily implemented using $4f$-shapers. We note that these numerical techniques can be generalized to implement unitary transformations on discrete frequency modes, with applications in classical signal processing and wavelength-division multiplexing [53,54].

Certain applications of mode sorting, such as quantum key distribution, require single-shot measurements. We use an analysis based on the likelihood ratio test to estimate the number of observations n required to discriminate the output Gaussian modes in Fig. 8. We estimate that a maximum of $n = 4$ and $n = 8$ observations are necessary to discriminate the Gaussians with 95% and 99% confidence, respectively (see Supplement 1, Section S3). The number of samples required for unambiguous discrimination of the Gaussians crucially depends on the chosen means and variances of the target modes. Supplement 1, Fig. S4 shows an additional instance of the temporal mode sorter where the separation of successive Gaussians has been doubled compared to that of the target modes shown in Fig. 8. With this increased separation, the target modes can be discriminated with single-shot measurements with 95% confidence, and with 99% confidence using $n = 2$ observations (see Supplement 1, Fig. S6.)

In order to implement our temporal mode sorter with single-photon states, it is necessary to minimize the required number of resources and the loss introduced by dispersive components in the path of the single photons. The complex temporal phases necessary in the four-stage mode sorter will be imparted to the single photons via the BS-FWM pumps. The losses due to dispersive components necessary to impart these phases on the BS-FWM pumps can be compensated with amplification as the pumps are classical. Each "time lens" stage of the temporal mode sorter introduces 1.3 dB loss (insertion loss of the BS-FWM setup). The other significant

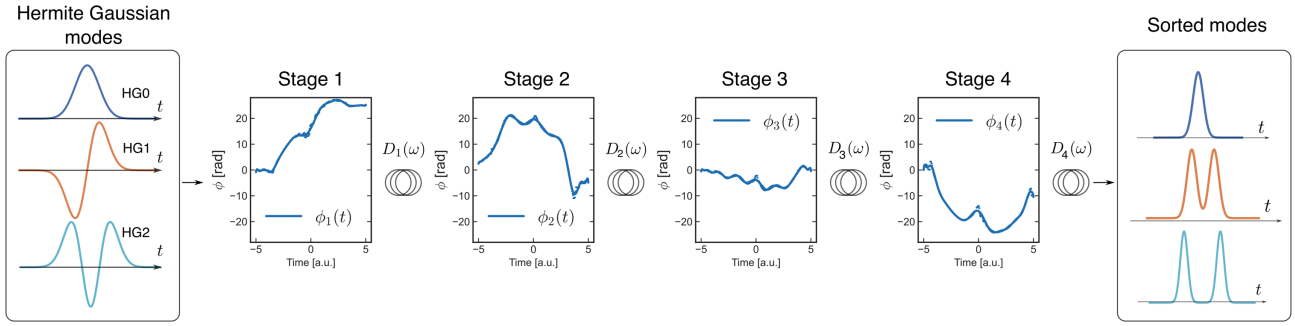

Fig. 7. Temporal mode sorting with a time lens. Complex, arbitrary unitary transformations on input temporal waveforms ψ_0^N are possible by cascading several time $\phi(t)$ and frequency $D(\omega)$ phase operations, as shown above. For temporal mode sorting, we set $\phi(t)$ to be an arbitrary time domain waveform and restrict $D(\omega)$ to second-order dispersion. The input waveforms ψ_0^N are an orthonormal basis set of N Hermite–Gaussian (HG) modes. The target waveforms are temporally separated Gaussian pulses. The parameters of ϕ and D are numerically optimized using steepest gradient descent to obtain maximum overlap for both forward ($\psi_{i,f}$) and backward ($\psi_{i,b}$) propagated waveforms at each stage i. Blue curves show optimized $\phi(t)$ for a four-stage, 10 HG mode sorter.

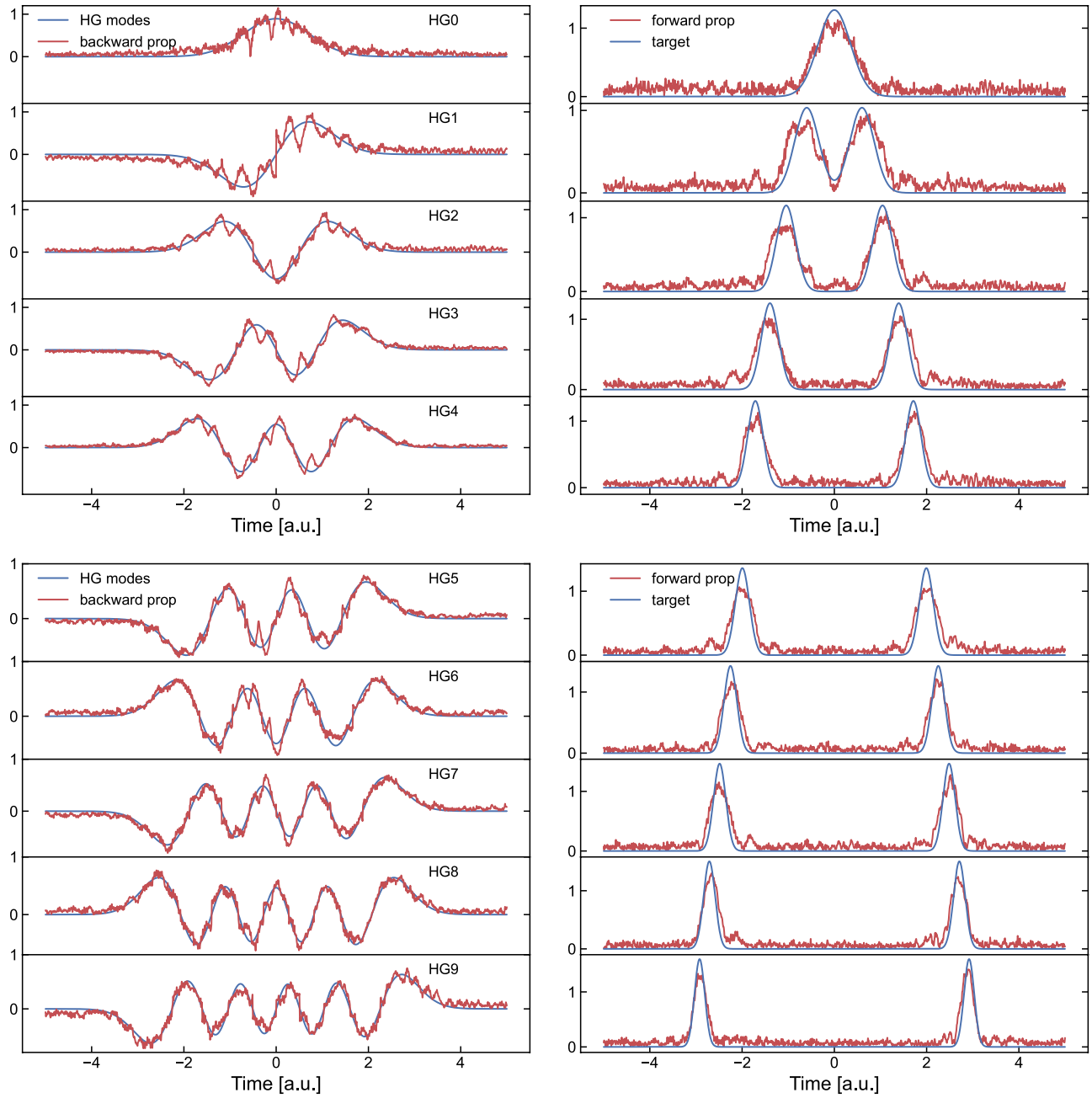

Fig. 8. Temporal mode sorting results. Sorting of 10 orthogonal 1D HG modes (left) to temporally separated Gaussians (right) using four cascaded stages of time and frequency phase manipulations. The blue curves denote the initial (left) and the target (right) modes, respectively. The red curves denote the backward (left) and forward propagated modes (right) from the target and initial modes, respectively. The optimization results in an overlap of 93% for the forward and backward propagated modes across all stages and all modes. The Gaussian pulses on the right can be temporally magnified and directly observed on single-photon detectors for efficient sorting/demultiplexing.

source of loss is second-order dispersion between each "time lens" stage. These stages mimic free-space propagation and must impart a large enough GDD Φ such that the condition $\Phi\delta\omega^2 \gg 1$ is satisfied. For pulses with bandwidth $\delta\omega = 2\pi \times 1$ THz, this condition is easily satisfied with $\Phi = 1-10$ ps^2. Similar to the temporal magnification setup, this can be achieved with 4–5 km of SMF fiber, resulting in 1.4 dB loss per sorting stage (see Supplement 1, Section S2). Our scheme can, therefore, be implemented with 3 dB loss per sorting stage. We note that, recently, the idea of temporal mode sorting with spectro-temporal transformations using EOMs has been discussed in [55]. Using simulated annealing, sorting of the first three HG modes is shown with a 12-stage mode transformation. With a conservative loss of 3 dB per sorting stage (typical commercial EOM insertion loss is 2–4 dB), this scheme introduces 36 dB loss in the path of the single photons and is infeasible for use with single-photon states (see Supplement 1, Section S2). In contrast, our approach provides a feasible path toward an experimental realization of a temporal mode sorter with $N = 10$ modes. Recently, integrated chirped Bragg gratings with broadband response and low propagation loss have been reported with both silicon nitride [56,57] and lithium niobate platforms [58]. These advances can provide compact,

scalable alternatives to fiber-based components for dispersion control and loss management.

6. CONCLUSION

In conclusion, we have demonstrated a single-photon-level time lens with picosecond resolution. Our temporal imaging system can overcome the intrinsic timing jitter of superconducting single-photon detectors and allows for temporal resolution for single-photon detection that approaches sub-picosecond. More advanced designs of SNSPDs with less than 50 ps timing jitter and photon-number resolving (PNR) capabilities are being developed using optimized nanowire designs and techniques for impedance matching [50,59,60]. Beyond temporal mode processing, the ability to process and detect quantum optical waveforms with THz-bandwidth opens new possibilities for high-dimensional quantum key distribution [61], quantum-enhanced sensing, and metrology [62,63]. It has been shown that two incoherent, spatially overlapping spots can be resolved with a resolution better than that set by Rayleigh's diffraction limit by measuring the image-plane field in the HG mode basis [64]. As shown in [64], such a measurement in the HG mode basis can saturate the quantum Cramér–Rao bound. A temporal mode sorter that demultiplexes just the first few HG modes can enable temporal pulse discrimination with a resolution superior to direct detection with dispersive optics using these theoretical insights. Our time-lens system can be used to perform unitary operations to manipulate the joint spectro-temporal correlations of time-frequency entangled (TFE) states, with applications in quantum-enhanced target detection [65]. Such manipulation and measurement of TFE states are crucial steps in protocols for quantum state discrimination, continuous variable super-dense coding, and illumination [62,66]. Combined with non-Gaussian PNR measurements and temporal mode interferometry, these applications can be extended to the generation and tomography of multipartite entangled cluster states [16,67–69]. Our time-lens approach can, thus, augment other all-optical techniques and provide a flexible framework for controlling and measuring the spectro-temporal degrees of freedom of high-bandwidth quantum states of light.

Funding. National Science Foundation (PHY-1707918, OMA-1936345); Australian Research Council (DE170100752).

Acknowledgment. B.M.S. acknowledges support from the Fulbright Future Scholarship (funded by the Kinghorn Foundation).

Disclosures. Certain commercial equipment and instruments are identified in this paper for completeness. Such identification does not imply recommendation or endorsement by the National Institute of Standards and Technology, nor does it imply that the materials or equipment identified are necessarily the best available for the purpose.

Data availability. Data underlying the results presented in this paper may be obtained from the authors upon reasonable request.

Supplemental document. See Supplement 1 for supporting content.

REFERENCES

1. C. Liu, Y. Sun, L. Zhao, S. Zhang, M. M. T. Loy, and S. Du, "Efficiently loading a single photon into a single-sided Fabry-Perot cavity," Phys. Rev. Lett. **113**, 133601 (2014).
2. L. Giannelli, T. Schmit, T. Calarco, C. P. Koch, S. Ritter, and G. Morigi, "Optimal storage of a single photon by a single intra-cavity atom," New J. Phys. **20**, 105009 (2018).
3. M. Heuck, K. Jacobs, and D. R. Englund, "Controlled-phase gate using dynamically coupled cavities and optical nonlinearities," Phys. Rev. Lett. **124**, 160501 (2020).
4. P. J. Bustard, R. Lausten, D. G. England, and B. J. Sussman, "Toward quantum processing in molecules: a THz-bandwidth coherent memory for light," Phys. Rev. Lett. **111**, 083901 (2013).
5. Q. Xu, P. Dong, and M. Lipson, "Breaking the delay-bandwidth limit in a photonic structure," Nat. Phys. **3**, 406–410 (2007).
6. D. Kielpinski, J. F. Corney, and H. M. Wiseman, "Quantum optical waveform conversion," Phys. Rev. Lett. **106**, 130501 (2011).
7. N. Matsuda, "Deterministic reshaping of single-photon spectra using cross-phase modulation," Sci. Adv. **2**, e1501223 (2016).
8. O. Morin, M. Körber, S. Langenfeld, and G. Rempe, "Deterministic shaping and reshaping of single-photon temporal wave functions," Phys. Rev. Lett. **123**, 133602 (2019).
9. J.-P. W. MacLean, J. M. Donohue, and K. J. Resch, "Direct characterization of ultrafast energy-time entangled photon pairs," Phys. Rev. Lett. **120**, 053601 (2018).
10. V. Ansari, J. M. Donohue, B. Brecht, and C. Silberhorn, "Tailoring nonlinear processes for quantum optics with pulsed temporal-mode encodings," Optica **5**, 534–550 (2018).
11. S. Ast, M. Mehmet, and R. Schnabel, "High-bandwidth squeezed light at 1550 nm from a compact monolithic PPKTP cavity," Opt. Express **21**, 13572–13579 (2013).
12. N. Takanashi, A. Inoue, T. Kashiwazaki, T. Kazama, K. Enbutsu, R. Kasahara, T. Umeki, and A. Furusawa, "All-optical phase-sensitive detection for ultra-fast quantum computation," Opt. Express **28**, 34916–34926 (2020).
13. T. Kashiwazaki, N. Takanashi, T. Yamashima, T. Kazama, K. Enbutsu, R. Kasahara, T. Umeki, and A. Furusawa, "Continuous-wave 6-dB-squeezed light with 2.5-THz-bandwidth from single-mode PPLN waveguide," APL Photon. **5**, 036104 (2020).
14. D. Bunandar, A. Lentine, C. Lee, H. Cai, C. M. Long, N. Boynton, N. Martinez, C. DeRose, C. Chen, M. Grein, D. Trotter, A. Starbuck, A. Pomerene, S. Hamilton, F. N. C. Wong, R. Camacho, P. Davids, J. Urayama, and D. Englund, "Metropolitan quantum key distribution with silicon photonics," Phys. Rev. X **8**, 021009 (2018).
15. J. Nunn, L. J. Wright, C. Söller, L. Zhang, I. A. Walmsley, and B. J. Smith, "Large-alphabet time-frequency entangled quantum key distribution by means of time-to-frequency conversion," Opt. Express **21**, 15959–15973 (2013).
16. P. C. Humphreys, W. S. Kolthammer, J. Nunn, M. Barbieri, A. Datta, and I. A. Walmsley, "Continuous-variable quantum computing in optical time-frequency modes using quantum memories," Phys. Rev. Lett. **113**, 130502 (2014).
17. D. V. Reddy, M. G. Raymer, C. J. McKinstrie, L. Mejling, and K. Rottwitt, "Temporal mode selectivity by frequency conversion in second-order nonlinear optical waveguides," Opt. Express **21**, 13840–13863 (2013).
18. D. V. Reddy, M. G. Raymer, and C. J. McKinstrie, "Sorting photon wave packets using temporal-mode interferometry based on multiple-stage quantum frequency conversion," Phys. Rev. A **91**, 012323 (2015).
19. B. Brecht, A. Eckstein, A. Christ, H. Suche, and C. Silberhorn, "From quantum pulse gate to quantum pulse shaper—engineered frequency conversion in nonlinear optical waveguides," New J. Phys. **13**, 065029 (2011).
20. B. Brecht, D. V. Reddy, C. Silberhorn, and M. G. Raymer, "Photon temporal modes: a complete framework for quantum information science," Phys. Rev. X **5**, 041017 (2015).
21. J. B. Christensen, D. V. Reddy, C. J. McKinstrie, K. Rottwitt, and M. G. Raymer, "Temporal mode sorting using dual-stage quantum frequency conversion by asymmetric Bragg scattering," Opt. Express **23**, 23287–23301 (2015).
22. V. Ansari, J. M. Donohue, M. Allgaier, L. Sansoni, B. Brecht, J. Roslund, N. Treps, G. Harder, and C. Silberhorn, "Tomography and purification of the temporal-mode structure of quantum light," Phys. Rev. Lett. **120**, 213601 (2018).
23. M. G. Raymer, D. V. Reddy, S. J. van Enk, and C. J. McKinstrie, "Time reversal of arbitrary photonic temporal modes via nonlinear optical frequency conversion," New J. Phys. **20**, 053027 (2018).
24. D. V. Reddy and M. G. Raymer, "High-selectivity quantum pulse gating of photonic temporal modes using all-optical Ramsey interferometry," Optica **5**, 423–428 (2018).

25. J. M. Donohue, M. Agnew, J. Lavoie, and K. J. Resch, "Coherent ultrafast measurement of time-bin encoded photons," Phys. Rev. Lett. **111**, 153602 (2013).
26. B. H. Kolner and M. Nazarathy, "Temporal imaging with a time lens," Opt. Lett. **14**, 630–631 (1989).
27. J. van Howe and C. Xu, "Ultrafast optical signal processing based upon space-time dualities," J. Lightwave Technol. **24**, 2649–2662 (2006).
28. R. Salem, M. A. Foster, A. C. Turner, D. F. Geraghty, M. Lipson, and A. L. Gaeta, "Optical time lens based on four-wave mixing on a silicon chip," Opt. Lett. **33**, 1047–1049 (2008).
29. Y. Okawachi, R. Salem, M. A. Foster, A. C. Turner-Foster, M. Lipson, and A. L. Gaeta, "High-resolution spectroscopy using a frequency magnifier," Opt. Express **17**, 5691–5697 (2009).
30. R. Salem, M. A. Foster, and A. L. Gaeta, "Application of space–time duality to ultrahigh-speed optical signal processing," Adv. Opt. Photon. **5**, 274–317 (2013).
31. M. Karpiński, M. Jachura, L. J. Wright, and B. J. Smith, "Bandwidth manipulation of quantum light by an electro-optic time lens," Nat. Photonics **11**, 53–57 (2017).
32. F. Sośnicki, M. Mikołajczyk, A. Golestani, and M. Karpiński, "Aperiodic electro-optic time lens for spectral manipulation of single-photon pulses," Appl. Phys. Lett. **116**, 234003 (2020).
33. J. M. Donohue, M. Mastrovich, and K. J. Resch, "Spectrally engineering photonic entanglement with a time lens," Phys. Rev. Lett. **117**, 243602 (2016).
34. O. Bryngdahl, "Geometrical transformations in optics," J. Opt. Soc. Am. **64**, 1092–1094 (1974).
35. G. C. G. Berkhout, M. P. J. Lavery, J. Courtial, M. W. Beijersbergen, and M. J. Padgett, "Efficient sorting of orbital angular momentum states of light," Phys. Rev. Lett. **105**, 153601 (2010).
36. N. K. Fontaine, R. Ryf, H. Chen, D. T. Neilson, K. Kim, and J. Carpenter, "Laguerre-Gaussian mode sorter," Nat. Commun. **10**, 1865 (2019).
37. M. Mirhosseini, M. Malik, Z. Shi, and R. W. Boyd, "Efficient separation of the orbital angular momentum eigenstates of light," Nat. Commun. **4**, 2781 (2013).
38. X. Pan, S. Yu, Y. Zhou, K. Zhang, K. Zhang, S. Lv, S. Li, W. Wang, and J. Jing, "Orbital-angular-momentum multiplexed continuous-variable entanglement from four-wave mixing in hot atomic vapor," Phys. Rev. Lett. **123**, 070506 (2019).
39. D. A. B. Miller, "Sorting out light," Science **347**, 1423–1424 (2015).
40. A. Farsi, "Coherent manipulation of light in the classical and quantum regimes via four-wave mixing Bragg scattering," Ph.D. thesis (Cornell University, 2015).
41. S. Clemmen, A. Farsi, S. Ramelow, and A. L. Gaeta, "Ramsey interference with single photons," Phys. Rev. Lett. **117**, 223601 (2016).
42. C. Joshi, A. Farsi, S. Clemmen, S. Ramelow, and A. L. Gaeta, "Frequency multiplexing for quasi-deterministic heralded single-photon sources," Nat. Commun. **9**, 847 (2018).
43. C. Joshi, A. Farsi, A. Dutt, B. Y. Kim, X. Ji, Y. Zhao, A. M. Bishop, M. Lipson, and A. L. Gaeta, "Frequency-domain quantum interference with correlated photons from an integrated microresonator," Phys. Rev. Lett. **124**, 143601 (2020).
44. H. J. McGuinness, M. G. Raymer, C. J. McKinstrie, and S. Radic, "Quantum frequency translation of single-photon states in a photonic crystal fiber," Phys. Rev. Lett. **105**, 093604 (2010).
45. L. Mejling, D. S. Cargill, C. J. McKinstrie, K. Rottwitt, and R. O. Moore, "Effects of nonlinear phase modulation on Bragg scattering in the low-conversion regime," Opt. Express **20**, 27454–27475 (2012).
46. C. J. McKinstrie, J. D. Harvey, S. Radic, and M. G. Raymer, "Translation of quantum states by four-wave mixing in fibers," Opt. Express **13**, 9131–9142 (2005).
47. C. J. McKinstrie, S. Radic, and M. G. Raymer, "Quantum noise properties of parametric amplifiers driven by two pump waves," Opt. Express **12**, 5037–5066 (2004).
48. C. J. McKinstrie, M. Yu, M. G. Raymer, and S. Radic, "Quantum noise properties of parametric processes," Opt. Express **13**, 4986–5012 (2005).
49. G. Agrawal, "Group-velocity dispersion," in *Nonlinear Fiber Optics*, 5th ed., Optics and photonics (Academic, 2013), Chap. 3, pp. 57–85.
50. B. Korzh, Q.-Y. Zhao, J. P. Allmaras, *et al.*, "Demonstration of sub-3 ps temporal resolution with a superconducting nanowire single-photon detector," Nat. Photonics **14**, 250–255 (2020).
51. M. Colangelo, A. Beyer, B. Korzh, *et al.*, "Impedance-matched differential SNSPDs for practical photon counting with sub-10 ps timing jitter," in *Conference on Lasers and Electro-Optics (CLEO)* (2021).
52. D. V. Reddy and M. G. Raymer, "Engineering temporal-mode-selective frequency conversion in nonlinear optical waveguides: from theory to experiment," Opt. Express **25**, 12952–12966 (2017).
53. S. Buddhiraju, A. Dutt, M. Minkov, I. A. D. Williamson, and S. Fan, "Arbitrary linear transformations for photons in the frequency synthetic dimension," Nat. Commun. **12**, 2401 (2021).
54. M. Mazur, N. K. Fontaine, H. Chen, R. Ryf, D. T. Neilson, G. Raybon, A. Adamiecki, S. Corteselli, and J. Schröder, "Multi-channel comb modulation in single waveguide structures," in *European Conference on Optical Communications (ECOC)* (2020), pp. 1–4.
55. J. Ashby, V. Thiel, M. Allgaier, P. d'Ornellas, A. O. C. Davis, and B. J. Smith, "Temporal mode transformations by sequential time and frequency phase modulation for applications in quantum information science," Opt. Express **28**, 38376–38389 (2020).
56. Z. Chen, J. Flueckiger, X. Wang, F. Zhang, H. Yun, Z. Lu, M. Caverley, Y. Wang, N. A. F. Jaeger, and L. Chrostowski, "Spiral Bragg grating waveguides for TM mode silicon photonics," Opt. Express **23**, 25295–25307 (2015).
57. Z. Du, C. Xiang, T. Fu, M. Chen, S. Yang, J. E. Bowers, and H. Chen, "Silicon nitride chirped spiral Bragg grating with large group delay," APL Photon. **5**, 101302 (2020).
58. M. Yu, C. Reimer, D. Barton, P. Kharel, R. Cheng, L. He, L. Shao, D. Zhu, Y. Hu, H. R. Grant, L. Johansson, Y. Okawachi, A. L. Gaeta, M. Zhang, and M. Lončar, "Femtosecond pulse generation via an integrated electro-optic time lens," arXiv:2112.09204 [physics] (2021).
59. D. V. Reddy, D. V. Reddy, R. R. Nerem, S. W. Nam, R. P. Mirin, and V. B. Verma, "Superconducting nanowire single-photon detectors with 98% system detection efficiency at 1550 nm," Optica **7**, 1649–1653 (2020).
60. D. Zhu, M. Colangelo, C. Chen, B. A. Korzh, F. N. C. Wong, M. D. Shaw, and K. K. Berggren, "Resolving photon numbers using a superconducting nanowire with impedance-matching taper," Nano Lett. **20**, 3858–3863 (2020).
61. J. Mower, Z. Zhang, P. Desjardins, C. Lee, J. H. Shapiro, and D. Englund, "High-dimensional quantum key distribution using dispersive optics," Phys. Rev. A **87**, 062322 (2013).
62. Q. Zhuang, Z. Zhang, and J. H. Shapiro, "Optimum mixed-state discrimination for noisy entanglement-enhanced sensing," Phys. Rev. Lett. **118**, 040801 (2017).
63. M. Shah and L. Fan, "Frequency superresolution with spectrotemporal shaping of photons," Phys. Rev. Appl. **15**, 034071 (2021).
64. M. Tsang, R. Nair, and X.-M. Lu, "Quantum theory of superresolution for two incoherent optical point sources," Phys. Rev. X **6**, 031033 (2016).
65. Y. Zhang, D. England, A. Nomerotski, P. Svihra, S. Ferrante, P. Hockett, and B. Sussman, "Multidimensional quantum-enhanced target detection via spectrotemporal-correlation measurements," Phys. Rev. A **101**, 053808 (2020).
66. H. Liu and A. S. Helmy, "Joint measurement of time–frequency entanglement via sum frequency generation," npj Quantum Inf. **6**, 66 (2020).
67. R. Nehra, A. Win, M. Eaton, R. Shahrokhshahi, N. Sridhar, T. Gerrits, A. Lita, S. W. Nam, and O. Pfister, "State-independent quantum state tomography by photon-number-resolving measurements," Optica **6**, 1356–1360 (2019).
68. R. Yang, J. Zhang, I. Klich, C. González-Arciniegas, and O. Pfister, "Spatiotemporal graph states from a single optical parametric oscillator," Phys. Rev. A **101**, 043832 (2020).
69. G. S. Thekkadath, M. E. Mycroft, B. A. Bell, C. G. Wade, A. Eckstein, D. S. Phillips, R. B. Patel, A. Buraczewski, A. E. Lita, T. Gerrits, S. W. Nam, M. Stobińska, A. I. Lvovsky, and I. A. Walmsley, "Quantum-enhanced interferometry with large heralded photon-number states," npj Quantum Inf. **6**, 89 (2020).